NOVEMBER 27 2023

Experimental and quantitative evaluation of frequency modulation caused by Doppler effect around high-speed moving sound source

Mariko Akutsu; Toki Uda; Yasuhiro Oikawa

J. Acoust. Soc. Am. 154, 3403–3413 (2023)
https://doi.org/10.1121/10.0022537

JASA ARTICLE

Experimental and quantitative evaluation of frequency modulation caused by Doppler effect around high-speed moving sound source

Mariko Akutsu,[1,2,a)] Toki Uda,[1] and Yasuhiro Oikawa[2]
[1]*Environmental Engineering Division, Railway Technical Research Institute, Kokubunji-shi, Tokyo 185-8540, Japan*
[2]*Department of Intermedia Art and Science, Waseda University, Shinjuku-ku, Tokyo 169-8555, Japan*

ABSTRACT:
High-speed train noise remains a wayside environmental issue. For accurate noise prediction, the characteristics of a moving sound source must be revealed. In this work, the frequency modulation of sound waves emitted from a high-speed moving sound source was experimentally investigated. In the experiment, the sound field around a running train model emitting a 40 kHz pure tone was measured by an optical measurement technique, parallel phase-shifting interferometry, which can visualize instantaneous sound fields. For quantitative evaluation, a lens distortion correction was also developed and adopted for the visualization results. From the measured result of a sound source moving at a running speed of 280 km/h, the frequency modulation, known as the Doppler effect, was observed, and the measured frequency agreed well with the theoretical values. © *2023 Acoustical Society of America*.
https://doi.org/10.1121/10.0022537
(Received 9 May 2023; revised 15 August 2023; accepted 9 November 2023; published online 27 November 2023)
[Editor: Andi Petculescu] Pages: 3403–3413

I. INTRODUCTION

Railway noise remains a wayside environmental issue. In Japan, the government has imposed environmental quality standards for the Shinkansen superexpress railway noise,[1] in which the maximum noise levels of Shinkansen wayside noise were set.[2] In planning new railway lines and increasing running speed, proper noise prediction is necessary. Since railway noise sources are distributed along rails and propagate as multiple moving sound sources, understanding the characteristics of moving sound sources allows us to achieve accurate noise prediction and efficient countermeasures. Thus, developing a noise prediction method according to various vehicles and geometries of railway structures is important. The Railway Technical Research Institute, Japan (RTRI), has developed a noise prediction model considering the effects of the heights of noise barriers or viaducts, etc.[3] In this model, sound sources are assumed as lined omnidirectional point sound sources. Other than the Shinkansen railways, a guideline of railway noise for the reconstruction of conventional Japanese lines was also established by the government.[4] For conventional lines, a noise prediction model with line sound sources[5] and point sound sources[6] was proposed.

In the European Union (EU), the European Directive of Environmental Noise (2002/49/EC)[7] requires a noise map of primary noise, including railway noise, which is assessed in an equivalent noise level.[8] To achieve the directive, a noise assessment method known as CNOSSOS-EU was developed.[9] In this method, railway noise is assumed to be a line source.

In both the Japanese and EU noise prediction models, noise sources are assumed to be stationary: i.e., the effects of moving sound sources are ignored. In general, when a sound source is moving, the wavelength of the sound waves emitted in the forward direction should become shorter, while the wavelength of those emitted in the backward direction becomes longer. As a result, the frequency of the sound is modulated depending on its speed, known as the Doppler effect. At the same time, the amplitude of the sound also varies in this situation.[10] Previous studies on those properties of the sound emitted from a moving sound source have been conducted. Doi investigated the noise levels of time series influenced by the time constant and the speed of the sound source.[11] Tsuru *et al.* simulated the distributions of a moving sound source with digital signal processing.[12] Furthermore, Duhamel proposed a three-dimensional calculation method for sound propagation, which offers less calculation time upon the expansion of a two-dimensional analysis.[13] Applying Duhamel's method to a moving sound source, Ogata estimated the insertion loss of noise barriers,[14] and Nakajima assessed numerical calculation errors.[15] Considering these findings about the moving sound source, Makino revealed that both the maximum noise level (Japanese assessment) and the equivalent noise level (EU assessment) of moving sound sources are larger than those of stationary sound sources,[16] indicating that these prediction models still have room for improvement by considering the effect of moving sound sources. The aforementioned previous studies related to a moving sound source are almost

[a)]Email: akutsu.mariko.82@rtri.or.jp

all theoretical or numerical simulations, and very few experimental studies have been conducted because employing real-time measurement methods of the two-dimensional (2D) sound field is difficult. Although applying the theoretical Doppler effect would be the simplest way in implementing the moving effect, in an actual train, the boundary layer formed around train vehicles could affect the sound field. This effect of the boundary layer is complex and remains unclear. Thus, as a first step towards understanding the actual sound propagation, we studied the visualization of the sound field around a moving sound source directly.[17–19]

Many optical methods have been proposed for visualizing the flow field, such as shadowgraph, schlieren method, background oriented schlieren method, and interferometry.[20,21] Optical measurement methods are currently being developed to measure airborne sound. The principle is as follows. When a laser light passes through the sound field, the phase of the laser light is affected by variations in the density of air (i.e., sound). This interaction between the laser light and sound is known as the acousto-optic effect. For example, the schlieren method, which is used for flow visualization, can also be utilized for qualitatively visualizing small density variations caused by audible sound after image processing.[22] In particular, ultrasonic waves with high-pressure gradients can be visualized in real time.[23] Other than the schlieren method, the Fraunhofer diffraction method[24] and a laser Doppler vibrometer[25–27] were proposed for measuring airborne sound. Interferometers, which measure air pressure fluctuations based on the phase difference between the reference laser light and object laser light,[28–31] have been studied for sound field measurements.[32,33] Parallel phase-shifting interferometry (PPSI) was also proposed for measuring sound. By utilizing a Fizeau-type polarized interferometer and a high-speed polarization camera, this methodology can measure the instantaneous sound field where the interferometer's laser passes through.[34–41] PPSI offers two merits: phases can be recorded highly accurately and quantitively since the high-speed polarization camera with multipolarization (four polarizations in this study) records the data at the same time, and instantaneous two-dimensional information can be captured with a single shot using a high-speed polarization camera.

In this paper, we experimentally investigated the frequency modulation of the Doppler effect around a moving sound source. To obtain the frequency distribution, PPSI was used for measuring the sound field. We also propose a lens distortion correction method to quantitatively evaluate the visualization results obtained using PPSI. The results showed that modulated frequencies agreed well with the theoretical values.

The rest of the paper is organized as follows: In Sec. II, we describe the acousto-optic measurement system, i.e., PPSI. In Sec. III, we explain our measurement setup for a high-speed moving sound source. In Sec. IV, we propose a lens distortion calibration method. Finally, in Sec. V, the measured frequencies are discussed, and the conclusions are presented in Sec. VI.

II. PARALLEL PHASE-SHIFTING INTERFEROMETER

A. Relationship between light phase and sound pressure

At position $\boldsymbol{r}$ and time t, the refractive index, n, changes with the air density. The refractive index is described by the Gladstone–Dale equation[42,43] as follows:

$$n(\boldsymbol{r},t) = K(\rho_0 + \rho) + 1, \tag{1}$$

where ρ_0 is the air density in the atmosphere, ρ is the fluctuation of the air density, and K is a constant, which depends on the type of gas and the wavelength of light. Under adiabatic change, the relationship between air density and sound pressure is expressed in terms of the specific heat ratio, γ, as follows:

$$\frac{p + p_0}{p_0} = \left(\frac{\rho + \rho_0}{\rho_0}\right)^{\gamma}, \tag{2}$$

and deformation to

$$\rho + \rho_0 = \rho_0\left(1 + \frac{p}{p_0}\right)^{1/\gamma}, \tag{3}$$

where p_0 is the atmospheric pressure, and p is the sound pressure. Substituting Eq. (3) into Eq. (1), we obtain

$$n(\boldsymbol{r},t) = K\rho_0\left(1 + \frac{p}{p_0}\right)^{1/\gamma} + 1. \tag{4}$$

Considering that the refractive index in the atmosphere is $n_0 = K\rho_0 + 1$, the following equation is obtained from Eq. (4):

$$n(\boldsymbol{r},t) = (n_0 - 1)\left(1 + \frac{p}{p_0}\right)^{1/\gamma} + 1. \tag{5}$$

Using the Taylor expansion, the second parentheses of the right can be described as

$$\left(1 + \frac{p}{p_0}\right)^{1/\gamma} = 1 + \frac{p}{\gamma p_0} + \frac{\left(\frac{1}{\gamma} - 1\right)}{2\gamma}\left(\frac{p}{p_0}\right)^2 + \cdots. \tag{6}$$

In general, atmospheric pressure is much greater than sound pressure; thus, only the first two terms in Eq. (6) are non-negligible. The relationship between refractive index and sound pressure is expressed as

$$n(\boldsymbol{r},t) = n_0 + \left(\frac{n_0 - 1}{\gamma p_0}\right)p(\boldsymbol{r},t). \tag{7}$$

Using the optical path length, φ, which is the integration along the path of the spatial line element, ds, the difference in the light phase, ϕ, is obtained by

https://doi.org/10.1121/10.0022537

$$\phi(\boldsymbol{r},t) = k\varphi = k\int_{L(\boldsymbol{r})} n(\boldsymbol{r},t)\,ds, \tag{8}$$

where k is the wavenumber and L is the propagation length of the laser light. Substituting Eq. (7) into Eq. (8), the following equation is obtained:

$$\phi(\boldsymbol{r},t) = kn_0\int_{L(\boldsymbol{r})} ds + k\left(\frac{n_0-1}{\gamma p_0}\right)\int_{L(\boldsymbol{r})} p(\boldsymbol{r},t)ds. \tag{9}$$

By replacing the integrated sound pressure, $\int_{L(\boldsymbol{r})} p(\boldsymbol{r},t)ds$, with $p_L(\boldsymbol{r},t)$, Eq. (9) can be rewritten as

$$\phi(\boldsymbol{r},t) = kn_0\int_{L(\boldsymbol{r})} ds + k\left(\frac{n_0-1}{\gamma p_0}\right)p_L(\boldsymbol{r},t). \tag{10}$$

From this equation, the integrated sound pressure is given by

$$p_L(\boldsymbol{r},t) = \frac{\gamma p_0}{k(n_0-1)}\phi(\boldsymbol{r},t) + C_{DC}, \tag{11}$$

$$C_{DC} = -\gamma p_0\frac{n_0}{n_0-1}\int_{L(\boldsymbol{r})} ds, \tag{12}$$

where C_{DC} is a time constant.

B. Measuring system using PPSI

As described by Eq. (11), the integrated sound pressure can be determined from the phase change of light. In this study, we utilized a phase measurement system, PPSI, which combining a parallel phase-shifting interferometer with a high-speed polarized camera for measuring the sound field. Figure 1 shows the schematic of the PPSI. First, the laser light is split into two orthogonal polarization lasers at the Wollaston prism. These lasers are expanded circularly and split into two lasers, reference and object light, at the beam splitter. Next, only the object light passes through the sound field and returns to the interferometer. Then, the returned object light is combined with the reference light at the beam splitter, and interference fringes are formed. Finally, the interference fringes are recorded by a high-speed polarization camera. In principle, the laser detects the accumulated fluctuations of the sound pressure; thus, the interference fringes include the integrated sound field along the laser path. The size of the measured area depends on the diameter of the reference plane, the mirror, and the lens behind the reference plane.

As shown in Fig. 1, the high-speed polarization camera incorporates a layer of polarizers above the image sensor. The polarizers comprise four angled filters (0, $\pi/4$, $\pi/2$, $3\pi/4$), enabling us to obtain interference fringes of four phases with a single shot. According to the Nyquist–Shannon theorem, the frame rate of the high-speed polarization camera is set to at least twice the frequency of the target sound.

In general, the light phase is estimated from the phase-shifted fringes obtained by sequentially recorded four phase-shifted fringes.[44] On the other hand, our system can record the four kinds of fringes simultaneously and have the advantage of the instantaneous measurements.[45] Although these methods need accurate phase-shift steps, it is difficult to perform them in practice. To overcome this problem, the hyper ellipse fitting in subspace (HEFS) method proposed by Yatabe[46,47] was used in our study. The HEFS method is a more accurate phase retrieval algorithm and developed by combining the ellipse fitting-based method and the subspace method. In addition, in the obtained phase distribution, phase unwrapping is necessary to eliminate the phase discontinuously between 2π and 0.[48] Also, the static phase needs to be eliminated. We also used the time-directional filtering method without phase unwrapping, which utilizes the wrapping operator and inverse filtering technique.[49]

III. VISUALIZATION OF SOUND FIELD AROUND A MOVING SOURCE

A. Low-noise moving model test facility

A low-noise moving model test facility at RTRI[50] was used to examine a high-speed moving sound source (Fig. 2). The facility was completed at RTRI in 2020 to evaluate micropressure waves that radiated from the train tunnel portal and low-frequency aerodynamic noise emitted during the

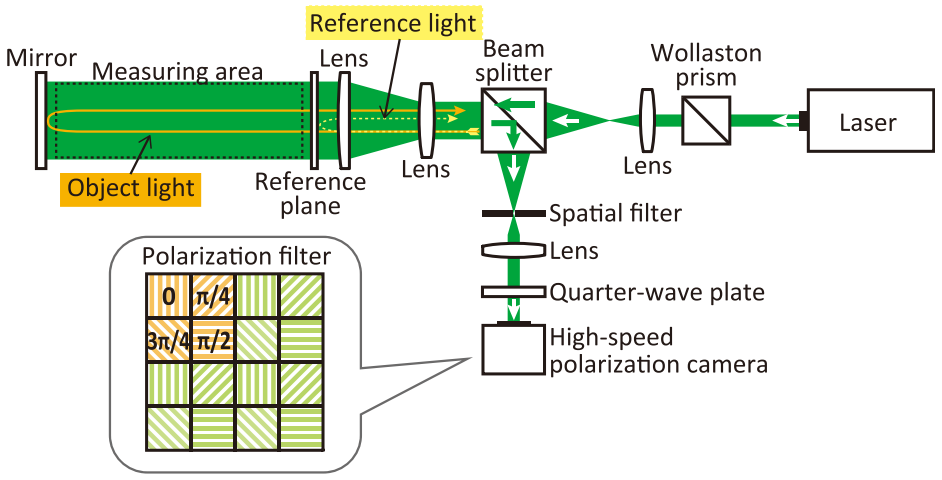

FIG. 1. (Color online) Schematic of the PPSI. The sound pressure fluctuations cause changes to the phase of the object light. The phase changes are recorded using a high-speed polarization camera as the interference fringes. Based on the principle of PPSI, the measured sound pressure represents the integrated sound pressure along the laser path.

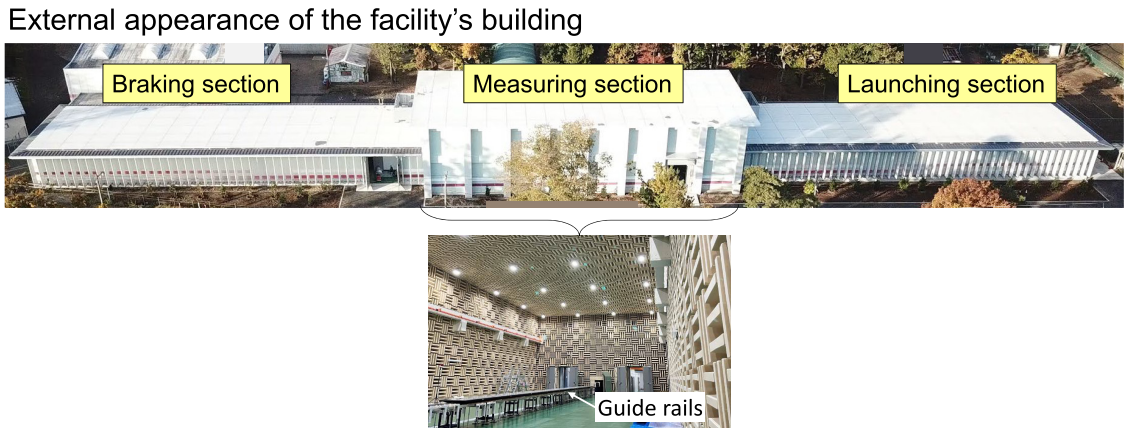

FIG. 2. (Color online) External appearance of the low-noise moving model test facility. This is a 125 m long test facility comprising launching, measuring, and braking sections. The measuring section is a semi-anechoic room with a length of 40 m. The train model runs on a pair of guide rails at a maximum speed of 400 km/h.

passage of the train. The train model can be accelerated to a maximum speed of 400 km/h. This facility is 125 m in length and involves launching, measuring, and braking sections. The train model is accelerated using roller rigs set in the launching section, and then, it enters the measuring section. The model runs on a pair of guide rails. The measuring section is a semi-anechoic room for acoustical measurement with a length of 40 m. After the measuring section, the train model is stopped using the frictional force of polystyrene beads in the braking section.

B. Experimental apparatus

In the low-noise moving model test facility, we visualized a sound field around a moving sound source mounted on a train model running at 100 km/h and 280 km/h. Figure 3 shows the positional relationship between the train model and PPSI. As a sound source, an ultrasonic transducer (PT40-18N; Nippon Ceramic Co., Ltd., Tottori, Japan.) emitting a 40 kHz pure tone was used. The wavelength is 8.5 mm, which is sufficient for visualization. The sound source was flush-mounted on the upper surface of the train model to propagate the sound upward, as shown in Fig. 3. The frequency of the sound source was 40 290 Hz and 116 dB at 175 mm above the source. Although the actual noise could have directivity, a monopole sound source was used in this fundamental study. The Shinkansen prediction model[3] also uses monopole sources as a sound source. Note that the directivity of the moving sound source was investigated in a previous study,[51] which measured directivities using a microphone set 175 mm above the upper surface of the train model and demonstrated good agreement with the theoretical directivities.

PPSI composed with an interferometer (DELTAPH PHI-100; Photonic Lattice, Inc., Sendai, Japan) and a high-speed polarization camera (CRYSTA PI-1P; Photonic Lattice, Inc.) were used for visualizing the sound field. The measurement instrument was arranged to measure the upper area of the train model where the sound propagates. The measurement area was 100 mm in diameter, which was inscribed in a rectangular area of 90×94 pixels. The frame rate of the high-speed polarization camera was 150 kfps.

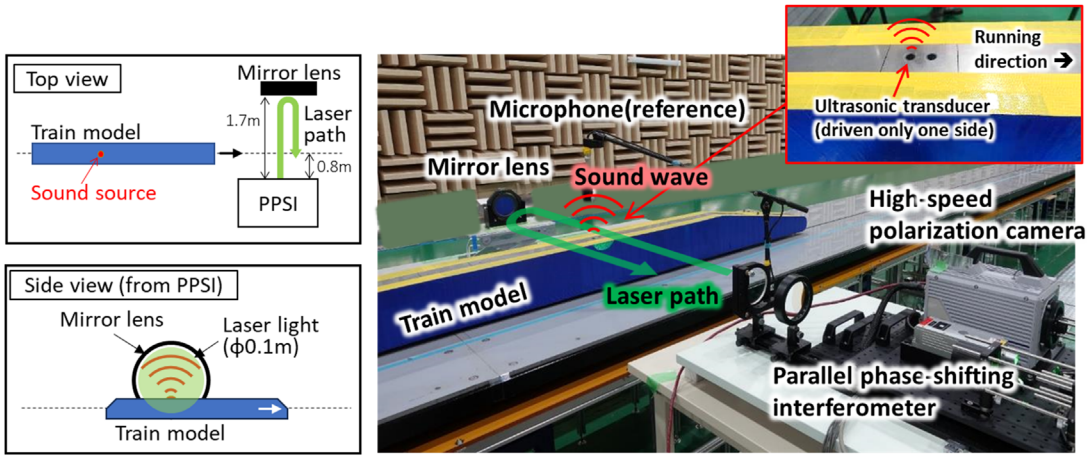

FIG. 3. (Color online) Positional relationship between the parallel phase-shifting interferometer and the train model. The sound source, i.e., an ultrasonic transducer, is flush-mounted on the upper surface of the train model to propagate the sound upward. The train model runs between the PPSI and the mirror lens. The measuring area was set to record the upper area of the train model, where the sound propagates. The laser axis is positioned perpendicular to the sound propagation direction.

https://doi.org/10.1121/10.0022537

C. Quantitative evaluation of the results

Figure 4 shows the visualization results of the sound field around a stationary sound source and moving sound sources at 100 km/h and 280 km/h. The color of the map corresponds to the relative sound pressure calculated from the first term in Eq. (11). Notably, since sound waves in the peripheral areas were affected by lens distortion, a distortion correction method was employed, as demonstrated in Sec. IV. Except for the peripheral area, propagating spherical waves were properly visualized. The results of the moving source [Figs. 4(a) and 4(b)] show that the wavelength in front of the source (i.e., the left side of the source) was shorter, and the wavelength behind the source (i.e., the right side of the source) was longer. This frequency modulation phenomenon is known as the Doppler effect. On the other hand, for a stationary source shown in Fig. 4(c), wavelengths were equal everywhere and do not depend on the positional relationship with the sound source.

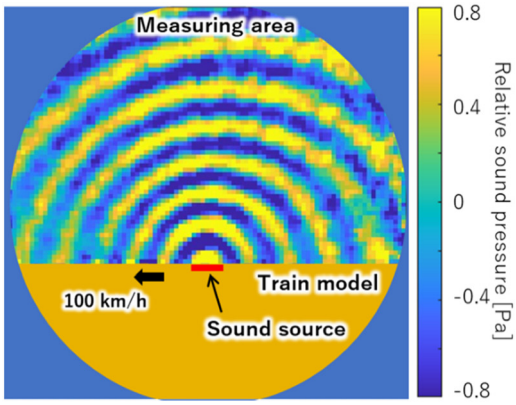

(a) Source at 100 km/h

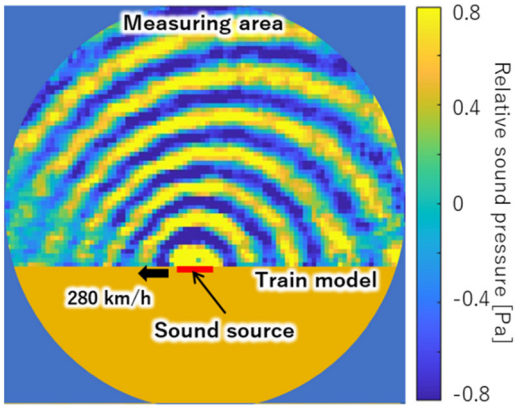

(b) Source at 280 km/h

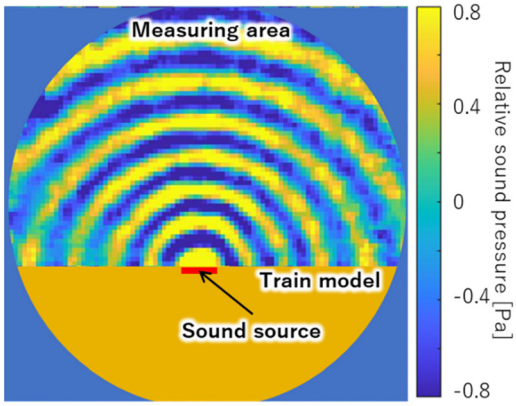

(c) Source at 0 km/h (static source)

FIG. 4. (Color online) Examples of visualization results. These figures show the frames when the sound source passes through the center of the measuring area. The lens distortion was present in the peripheral areas of these images. (a to c) Train model with the sound source moving right to left at 100 km/h (a) and 280 km/h (b), and a static model (c). As shown in figures, the wavelength of the sound waves in the vicinity of the moving source changes from position to position.

To observe variations in the frequency modulation, three types of time-directional bandpass filtering were applied to the results obtained at 280 km/h. These bandpass filters replaced the high-pass filter mentioned in Sec. II B. The characteristics of these bandpass filters are shown in Fig. 5, and the filtered results are shown in Fig. 6. Although the sound of approximately 40 kHz was radiated upward only, the sound higher and lower than 40 kHz was radiated to the front and rear of the sound source, respectively, indicating that the dependence of frequency distributions on the relative position to the sound source was clearly observed.

IV. CORRECTION OF LENS DISTORTION

A. Visualization of images with lens distortion

The visualization results of the interferometer are affected by lens distortion. For example, a straight stick placed on the right side is recognized as a slightly distorted object in Fig. 7. It is found that a radial distortion (pincushion distortion) is caused by the optical system used in this study. The elimination of distortions from the obtained images is required to evaluate the frequency modulation quantitatively. Therefore, we applied a calibration method developed for camera images to modify the visualization images. This is because the interference fringes were

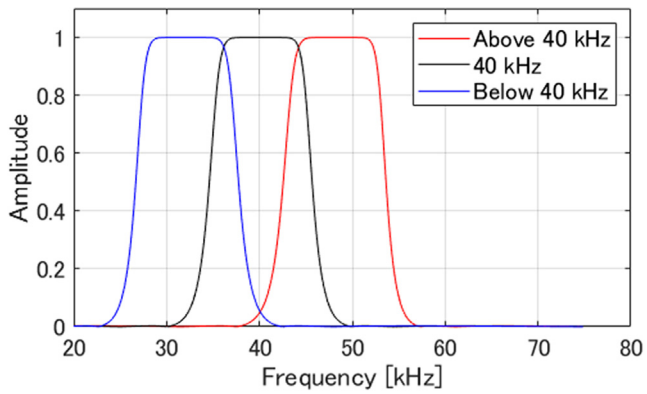

FIG. 5. (Color online) Characteristics of time-directional bandpass filters. Three filters were used in this study: less than 40 kHz, approximately 40 kHz, and higher than 40 kHz.

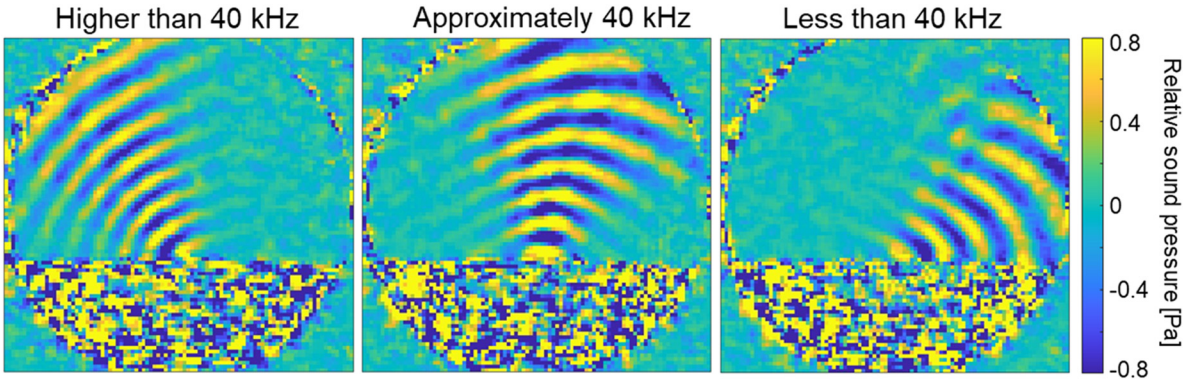

FIG. 6. (Color online) Filtered results of the three bandpass filters at 280 km/h. The sound approximately 40 kHz was radiated only upward. The sound higher or less than 40 kHz was radiated to the front or rear of the sound source.

captured by the image sensor of the high-speed polarization camera.

B. Correction method considering the coordinate system

In the PPSI results, the lens distortion is influential only in the radial direction, not in the tangential direction, since all lenses in the interferometer are installed parallel to each other. This section describes the distortion correction method used in the radial distortion.

The relationship between the world coordinate system and the PPSI coordinate system can be analogized in the relationship between the world coordinate system and the general camera coordinate system. By applying the pinhole camera model, the three-dimensional (3D) world coordinate is transformed to the camera coordinate as follows (Fig. 8):

$$s\tilde{\boldsymbol{m}} = \boldsymbol{A}[\boldsymbol{R}\,\boldsymbol{t}]\tilde{\boldsymbol{M}}, \tag{13}$$

$$\boldsymbol{A} = \begin{bmatrix} \alpha & 0 & u_0 \\ 0 & \beta & v_0 \\ 0 & 0 & 1 \end{bmatrix}, \tag{14}$$

where s is the scale factor, $\tilde{\boldsymbol{m}} = [u, v, 1]^T$ is the image point on the camera coordinate, $\boldsymbol{A}$ is an intrinsic parameter, α and β are scale factors in the u and v axes of the camera image, u_0 and v_0 are the coordinates of the optical center, $\boldsymbol{R} = [\boldsymbol{r}_1, \boldsymbol{r}_2, \boldsymbol{r}_3]$ is a rotation parameter, $\boldsymbol{t}$ is a translation parameter, and $\tilde{\boldsymbol{M}} = [X, Y, Z, 1]^T$ is a point on the 3D world coordinate. $\tilde{\boldsymbol{m}}$ and $\tilde{\boldsymbol{M}}$ are the homogeneous coordinates of $m = [u, v]^T$ and $M = [X, Y, Z]^T$. The matrix $[\boldsymbol{R}\,\boldsymbol{t}]$ is an extrinsic parameter.

Considering the radial distortion, the distorted camera coordinate moves in the radial direction. Thus, the distorted camera coordinate, $[\check{u}, \check{v}]$, is given as

$$\check{u} = u + (u - u_0)\left(k_1 r^2 + k_2 r^4\right), \tag{15}$$

$$\check{v} = v + (v - v_0)\left(k_1 r^2 + k_2 r^4\right), \tag{16}$$

where k_1 and k_2 are the radial distortion coefficients of the lens, $r^2 = x^2 + y^2$, and x and y are the normalized coordinates of the undistorted image.[52,53] Therefore, the intrinsic parameters, the extrinsic parameter, and the radial distortion coefficients need to be estimated for lens distortion correction.

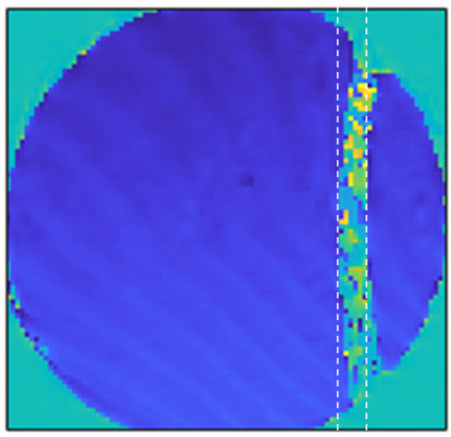

FIG. 7. (Color online) Visualization result of a straight stick. The stick was slightly distorted by lens distortion. The dotted lines indicate the actual position of the stick.

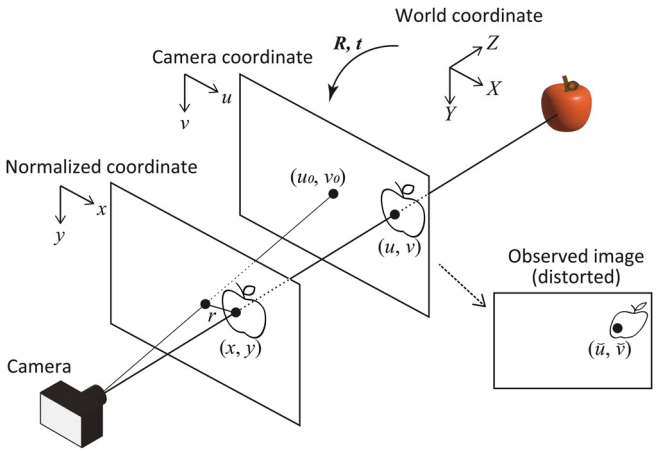

FIG. 8. (Color online) Relationships among various coordinate systems. An object in the world coordinate transforms to the camera coordinates via the extrinsic and intrinsic parameters.

https://doi.org/10.1121/10.0022537

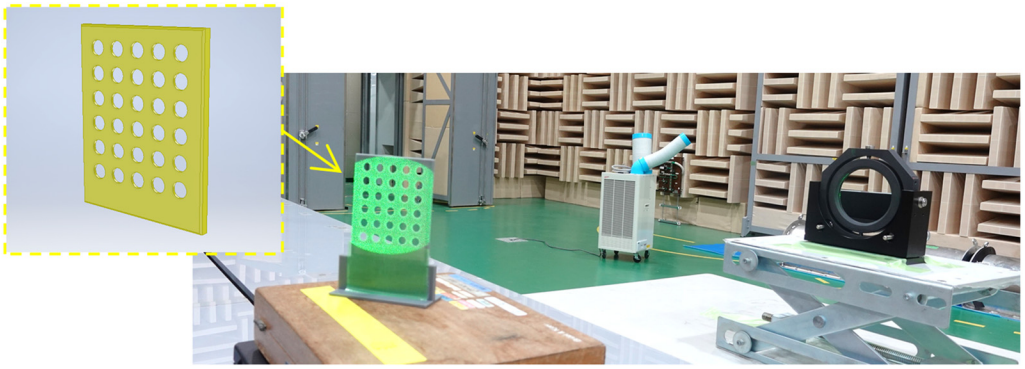

FIG. 9. (Color online) Calibration environment. The calibration plate with holes was set on the measured area, which is located between the interferometer and the mirror lens.

C. Correcting interferometer distortion

The visualization images of a dot pattern were used to estimate the intrinsic and extrinsic parameters and the radial distortion coefficients of Eq. (13). In this study, these parameters were estimated using Zhang's method, which uses pattern images for camera calibrations.[52] The actual calculations were performed using the "cameraParameters" MATLAB's function.[54]

A calibration plate with a dot pattern was fabricated using a 3D printer and visualized by the interferometer. Using a dot pattern is more suitable than the checkerboard pattern for the interferometer result with low spatial resolution since the position of each dot can be determined by the center of the gravity. The interference fringes appeared only at the dot holes where the laser passed through. The plate set on the measured area had 30 holes (6×5 holes) with spacings of 13 mm between holes, and each hole was 8 mm in diameter. Figure 9 shows the calibration plate and a scene of recording the plate. An averaged calibration image was generated using 1000 frames of phase images captured by the PPSI. One example of the phase images after averaging is shown in Fig. 10. In this figure, the center of the gravity of each hole, which corresponds to $\tilde{\boldsymbol{m}}$ in Eq. (13), is illustrated with cross-marks. We used two averaged calibration images with different angles of the calibration plate. To reconstruct the undistort image, a linear complement was used for pixel-to-pixel correction.

Visualization images are compared before and after correction. Figure 11 shows the results of the straight stick. It is obvious that the distorted stick was corrected to be straight by the distortion calibration. The sound waves from a stational sound source of 40 kHz are also shown in Fig. 12. In the uncorrected image, the wavefront near the periphery expands outwards. In the corrected image, on the other hand, the wavefront was approximately a half-circle. These results suggest that the calibration method works effectively for the visualization results of an interferometer.

V. FREQUENCY MODULATION OF THE DOPPLER EFFECT

In this section, frequency modulations around a sound source moving at 280 km/h are verified using the

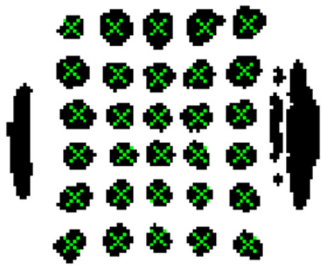

FIG. 10. (Color online) Averaged result of the calibration image. Black indicates the holes where the laser can pass through. Holes were clearly detected in the result. The X indicates the center of gravity in each hole.

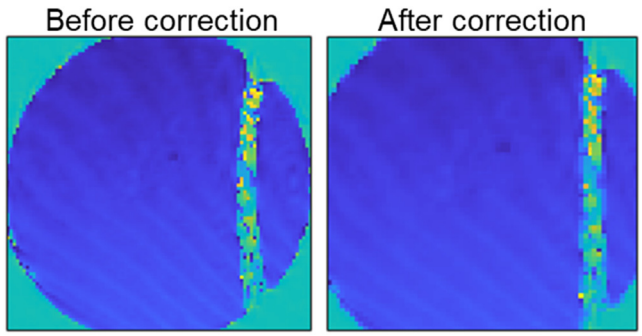

FIG. 11. (Color online) Distortion correction result of the straight stick. By applying the correction, the distortions of the stick were corrected to appear straight.

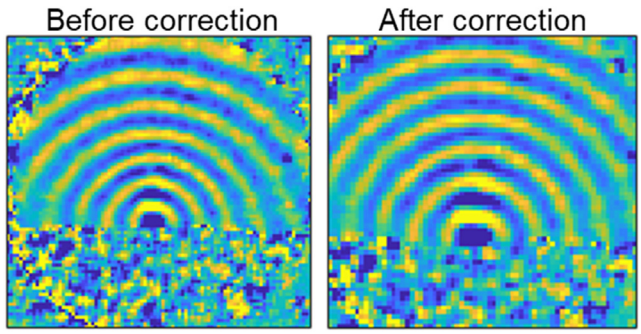

FIG. 12. (Color online) Distortion correction result of a stationary sound source of 40 kHz. By applying the correction, the distortions around the image edge were corrected.

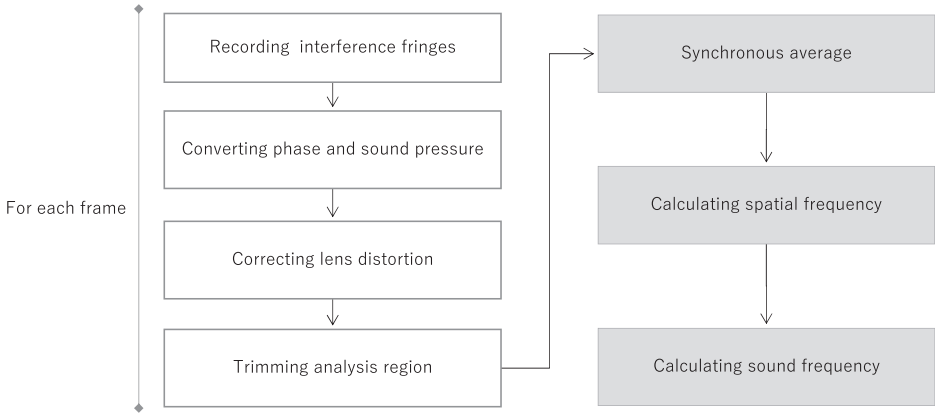

FIG. 13. Analysis flow chart to obtain sound frequencies using PPSI. The first to fourth steps (shown in the white box) are adopted for each frame.

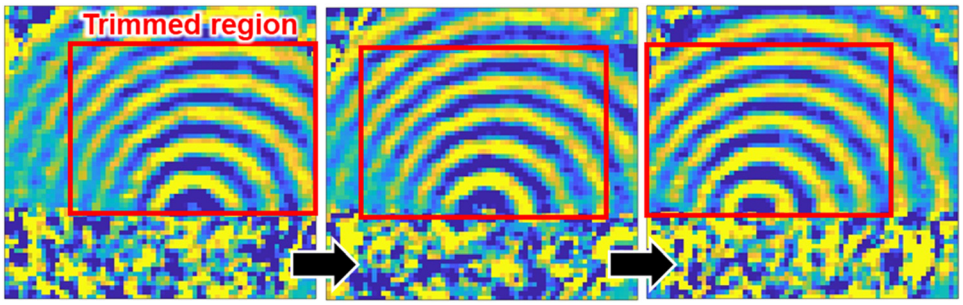

FIG. 14. (Color online) Example of the trimmed region. The analysis region was trimmed in the fourth step of the frequency calculation process (shown in Fig. 13). The trimmed region was determined based on the sound source position in subpixel order.

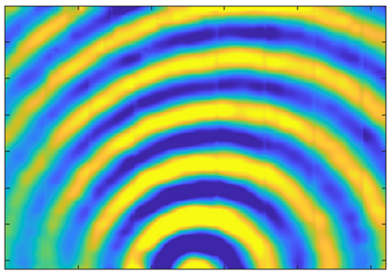

FIG. 15. (Color online) Averaged image. The synchronous average was adopted every 15 frames at the fifth step (shown in Fig. 13).

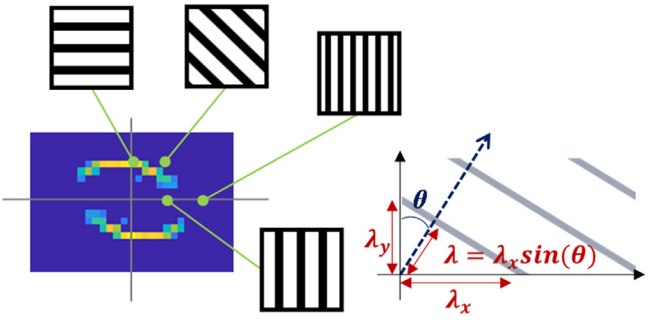

FIG. 17. (Color online) Schematic of the spatial frequency distribution. The spacing and tilt of the striped pattern that constructs the image are determined from the spatial frequency distribution. The wavelength of sound, λ, is obtained from the spatial frequency distribution.

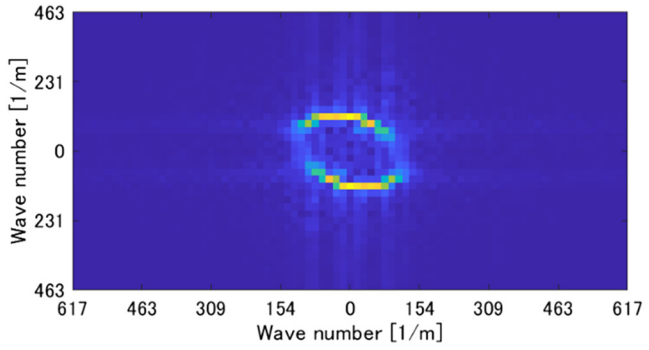

FIG. 16. (Color online) Spatial frequency distribution in Fig. 15. The blue to yellow color indicates the gain of the fast Fourier transform (FFT) results. The spatial frequency was calculated at the sixth step of the process illustrated in Fig. 13.

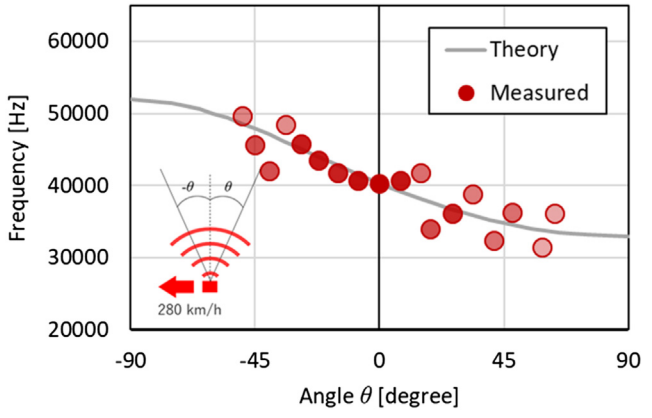

FIG. 18. (Color online) Frequency distribution around a sound source moving at 280 km/h. The red dot represents the measured frequency, and its intensity corresponds to the amplitude of the spatial frequency. The gray line represents the theoretical value calculated by Doppler's formula. The measured frequency modulation agrees with the theoretical value obtained using the Doppler effect.

https://doi.org/10.1121/10.0022537

visualization results mentioned in Sec. III C. Figure 13 shows a flow chart for obtaining frequencies from the visualization results. First, interference fringes recorded by the polarized high-speed camera are converted to the sound pressure by formulas presented in Sec. II A. After the lens distortion correction (described in Sec. IV), the analysis region is trimmed. The region depends on the position of the sound source in Fig. 14. To track the source position accurately, the visualized image is spatially up sampled, and the analysis region is decided in subpixel order. These four steps are applied to each frame of the images. Next, synchronous average processing is applied every 15 frames, which correspond to four cycles of 40 kHz sound. The average image is depicted in Fig. 15. Then, considering the sound wave forms' stripe pattern imagery, the spatial frequencies that indicate the wavelength and propagation direction of the sound, are calculated by two-dimensional fast Fourier transform. Finally, the sound frequency and propagation direction are calculated by the spatial frequency. The spatial frequency distribution of the result obtained at 280 km/h is shown in Fig. 16.

As shown in Fig. 17, the spatial frequency distribution represents the wave number and angle of stripe pattern. The horizontal axis represents the wavenumber of sound waves in the propagation direction of the train model, and the vertical axis represents the wavenumber in the vertical direction. The spatial distribution is symmetric with respect to the origin, and only the upper half of the y axis is used in this study. From this relationship between the spatial frequency distribution and sound information, the propagation direction and sound frequency are expressed as follows:

$$\theta = \begin{cases} 0, & \lambda_x = 0, \\ \tan^{-1}\dfrac{\lambda_y}{\lambda_x}, & \lambda_x \neq 0, \end{cases} \tag{17}$$

$$f_{\mathrm{meas}}(\theta) = \begin{cases} \dfrac{c}{\lambda_y}, & \theta = 0, \\ \dfrac{c}{\lambda_x \sin(\theta)}, & 0 < \theta \leq \dfrac{\pi}{2}. \end{cases} \tag{18}$$

Where θ is the angle from the line perpendicular to the sound source, λ is the wavelength of each axis (i.e., the distance of the stripe), and c is the speed of sound, which is 348.3 m/s (the temperature was 28 °C in the measurement room).

The theoretical value of the frequency modulation f_{theory} is calculated using the Doppler equation:

$$f_{\mathrm{theory}}(\theta) = f_0 \frac{c}{c \pm v \sin|\theta|}, \tag{19}$$

where f_0 is the original frequency of the sound source, and v is the velocity of the sound source. Note that negative θ means the observer is in front of the sound source, and positive θ means the observer is behind the source. The sign of v is the same as θ.

The sound frequency distribution around the sound source at 280 km/h obtained by the measurement is shown in Fig. 18. To calculate the frequency, values above 30% of the maximum amplitude shown in Fig. 16 were used. In Fig. 18, the color intensity of the plots represents the amplitude of the spatial frequency. Theoretical values calculated by Eq. (19) are added in Fig. 18, and the frequencies are modulated higher in front of the sound source and lower behind the source. The measured results show a similar trend compared with that of the theoretical values. The differences between the measured and theoretical results were smaller at larger amplitudes. In this study, the difference was within 5 kHz, which corresponds to 15% of the original frequency (40 kHz). These results reveal that the observed frequency modulation has the same trends as the theoretical one, indicating that frequencies around a high-speed moving sound source can be expressed using the Doppler equation.

VI. CONCLUSION

We experimentally investigated the frequency modulation around a high-speed moving sound source. The PPSI was used for visualizing sound waves. A lens distortion correction method was also developed for the visualized images. Using these methods, we quantitatively visualized sound waves around a moving sound source at 280 km/h. As a result, changes in the wavelength of the sound were clearly observed. Moreover, the frequency modulations analyzed from the visualization images agreed well with the theoretical values. Future work will focus on amplitude modulation around a moving sound source for a better understanding of the characteristics of a moving sound source like railway noise.

ACKNOWLEDGMENTS

This work was performed in collaboration with Waseda University, Kyoto University, and Railway Technical Research Institute.

[1]Ministry of the Environment, "Environmental quality standards for Shinkansen superexpress railway noise," in *Notification No. 91 of 1993* (Ministry of the Environment, Tokyo, 1993).
[2]S. Ono, "Measurement and analysis of railway noise in Japan," J. Acoust. Soc. Jpn. E **21**(6), 345–348 (2000).
[3]K. Nagakura and Y. Zenda, "Prediction model of wayside noise level of Shinkansen," in *Proceedings of the WAVE 2002 Workshop*, Yokohama, Japan (A A Balkema, Cape Town, Republic of South Africa, 2004), pp. 2563–2566.
[4]Ministry of the Environment, "Environmental quality guidelines for conventional railway noise," in *Notification No. 174 of 1995* (Ministry of the Environment, Tokyo, 1995).
[5]Y. Moritoh, K. Nagakura, H. Tachikawa, and S. Ogata, "Proposal of a prediction model for noise of conventional railway," J. INCE Jpn. **20**(3), 146–151 (1996) (in Japanese).
[6]T. Kobayashi, S. Yokoyama, H. Yano, and H. Tachibana, "Study on noise radiation characteristics of conventional railways," in *Proceedings of Internoise 2008: International Congress and Exposition on Noise Control Engineering*, Shanghai, China (October 26–29, 2008) (I-INCE, Luzern, Switzerland, 2008).
[7]European Commission Directive, *2002/49/EC of the European Parliament and of the Council of 25 June 2002 Relating to the Assessment and Management of Environmental Noise* (2002).

[8]R. R. K. Jones, "Recent developments in noise legislation and prediction methodologies for railways in Europe," Acoust. Sci. Technol. **28**(6), 367–374 (2007).
[9]S. Kephalopoulos, M. Paviotti, and F. Anfosso-Ledee, *Common Noise Assessment Methods in Europe (CNOSSOS-EU)* (Publications Office of the European Union, Luxembourg, 2012).
[10]M. E. Goldstein, *Aeroacoustics*, 1st ed. (McGraw-Hill, New York, 1976), pp. 45–53.
[11]T. Doi, M. Hiroe, and J. Kaku, "A study in the measurement of sound radiated from a high-speed moving source," in *Proceedings of the Spring Meeting of the Acoustical Society of Japan*, Kyoto, Japan (Acoustical Society of Japan, Tokyo, Japan, 1997), pp. 739–740 (in Japanese).
[12]H. Tsuru, H. Nakajima, and K. Takahashi, "Numerical simulation and auralization of moving sound source," in *Proceedings of the Autumn Meeting of the Acoustical Society of Japan*, Iwate, Japan (Acoustical Society of Japan, Tokyo, Japan, 2000), pp. 667–668 (in Japanese).
[13]D. Duhamel, "Efficient calculation of the three-dimensional sound pressure field around a noise barrier," J. Sound Vib. **197**(5), 547–571 (1996).
[14]S. Ogata, H. Tsuru, H. Nakajima, and K. Fujiwara, "Investigation for insertion loss of noise barrier for sound source moving at high speed," Acoust. Sci. Technol. **24**(3), 148–150 (2003).
[15]H. Nakajima, H. Tsuru, and S. Ogata, "Analysis and error investigation using Duhamel's efficient calculation of sound field produced by moving source," in *INTER-NOISE and NOISE-CON Congress and Conference Proceedings, Internoise05*, Rio de Janeiro, Brazil (2005) (I-INCE, Luzern, Switzerland, 2005), pp. 2343–2352.
[16]Y. Makino and Y. Takano, "Effect of sound source movement at low Mach number on radiated noise level," in *INTER-NOISE and NOISE-CON Congress and Conference Proceedings, Internoise21*, Washington, DC (2021), pp. 3731–3737.
[17]M. Akutsu, T. Uda, K. Yatabe, and Y. Oikawa, "Experimental observation of the sound field around a moving source using parallel phase-shifting interferometry," in *INTER-NOISE and NOISE-CON Congress and Conference Proceedings, Internoise22*, Glasgow, Scotland (2022), pp. 2999–3998, 3733–3739.
[18]M. Akutsu, T. Uda, K. Yatabe, and Y. Oikawa, "Visualization of sound waves around high-speed moving source using parallel phase-shifting interferometry," in *Proceedings of the 24th International Congress on Acoustics, ICA 2022*, Gyeongju, South Korea (2022) (International Commission for Acoustics, Madrid, Spain, 2022), p. abs-0277.
[19]M. Akutsu, T. Uda, K. Yatabe, and Y. Oikawa, "Visualization of sound wave from high-speed moving source," Acoust. Sci. Technol. **43**(6), 339–341 (2022).
[20]W. J. Yang and Y. Chen, "Optical methods in flow visualization," J. Laser Appl. **1**(4), 31–39 (1989).
[21]G. S. Settles and M. J. Hargather, "A review of recent developments in schlieren and shadowgraph techniques," Meas. Sci. Technol. **28**(4), 042001–042025 (2017).
[22]M. J. Hargather, G. S. Settles, and M. J. Madalis, "Schlieren imaging of loud sounds and weak shock waves in air near the limit of visibility," Shock Waves **20**(1), 9–17 (2010).
[23]A. Crockett and W. Rueckner, "Visualizing sound waves with schlieren optics," Am. J. Phys **86**(11), 870–876 (2018).
[24]Y. Sonoda and M. Akazaki, "Measurement of low-frequency ultrasonic waves by Fraunhofer diffraction," Jpn. J. Appl. Phys. **33**(5), 3110–3114 (1994).
[25]K. Nakamura, M. Hirayama, and S. Ueha, "Measurements of air-borne ultrasound by detecting the modulation in optical refractive index of air," in *Proceedings of the 2002 IEEE Ultrasonics Symposium*, Munich, Germany (IEEE, New York, 2002), Vol. 1, pp. 609–612.
[26]Y. Oikawa, M. Goto, Y. Ikeda, T. Takizawa, and Y. Yamasaki, "Sound field measurements based on reconstruction from laser projections," in *Proceedings of the IEEE International Conference on Acoustics, Speech, and Signal Processing, ICASSP05*, Philadelphia, PA (IEEE, New York, 2005), pp. 661–664.
[27]Y. Oikawa, T. Hasegawa, Y. Ouchi, Y. Yamasaki, and Y. Ikeda, "Visualization of sound field and sound source vibration using laser measurement method," in *Proceedings of the 20th International Congress on Acoustics, ICA 2010*, Sydney, Australia (2010) (International Congress on Acoustics, madrid, Spain, 2010), pp. 992–996.
[28]A. Torras-Rosell, S. Barrera-Figueroa, and F. Jacobsen, "Sound field reconstruction using acousto-optic tomography," J. Acoust. Soc. Am **131**(5), 3786–3793 (2012).
[29]R. Chevalerias, Y. Latron, and C. Veret, "Methods of interferometry applied to the visualization of flows in wind tunnels," J. Opt. Soc. Am. **47**(8), 703–706 (1957).
[30]G. Smeets, "Laser interferometer for high sensitivity measurements on transient phase objects," IEEE Trans. Aerosp. Electron. Syst. **AES-8**(2), 186–190 (1972).
[31]G. Smeets, "Flow diagnostics by laser interferometry," Aerosp. Electron. Syst. IEEE Trans. **AES-13**(2), 82–90 (1977).
[32]K. Takahashi, S. Hatano, K. Nagayama, S. Mohri, and Y. Asahara, "Optical measurement of sound field by laser differential interferometry," J. Vis. Soc. Jpn. **16**(1), 119–122 (1996) (in Japanese).
[33]B. Fischer and E. Wintner, "Sound recording by laser interferometry," in *2009 Conference on Lasers and Electro-Optics and 2009 Conference on Quantum Mechanics and Laser Science*, Baltimore, MD (IEEE, New York, 2009), pp. 1–2.
[34]K. Ishikawa, K. Yatabe, N. Chitanont, Y. Ikeda, Y. Oikawa, T. Onuma, H. Niwa, and M. Yoshii, "High-speed imaging of sound using parallel phase-shifting interferometry," Opt. Express **24**(12), 12922–12932 (2016).
[35]R. Tanigawa, K. Yatabe, and Y. Oikawa, "Guided-spatio-temporal filtering for extracting sound from optically measured images containing occluding objects," in *Proceedings of the 2019 International Conference on Acoustics, Speech, and Signal Processing. ICASSP 2019*, Brighton, UK (2019), pp. 945–949.
[36]R. Tanigawa, K. Yatabe, and Y. Oikawa, "Experimental visualization of aerodynamic sound sources using parallel phase-shifting interferometry," Exp. Fluids **61**, 206 (2020).
[37]K. Ishikawa, K. Yatabe, and Y. Oikawa, "Seeing the sound of castanets: Acoustic resonances between shells captured by high-speed optical visualization with 1-mm resolution," J. Acoust. Soc. Am. **148**(5), 3171–3180 (2020).
[38]K. Ishikawa, K. Yatabe, and Y. Oikawa, "Physical-model-based reconstruction of axisymmetric three-dimensional sound field from optical interferometric measurement," Meas. Sci. Technol. **32**(4), 045202 (2020).
[39]Y. Takase, K. Shimizu, S. Mochida, T. Inoue, K. Nishio, S. K. Rajput, O. Matoba, P. Xia, and Y. Awatsuji, "High-speed imaging of the sound field by parallel phase-shifting digital holography," Appl. Opt. **60**(4), A179–A187 (2021).
[40]S. Yoshida, R. Tanigawa, K. Yatabe, and Y. Oikawa, "Underwater sound visualization and temperature measurement using high-speed interferometer," Acoust. Sci. Technol. **43**(3), 177–187 (2022).
[41]D. Hermawanto, K. Ishikawa, K. Yatabe, and Y. Oikawa, "Determination of microphone acoustic center from sound field projection measured by optical interferometry," J. Acoust. Soc. Am. **153**(2), 1138–1146 (2023).
[42]J. H. Gladstone and T. P. Dale, "Researches on the refraction, dispersion, and sensitiveness of liquids," Philos. Trans. R. Soc. London **153**, 317–343 (1863).
[43]W. Merzkirch, *Techniques of Flow Visualization* (Advisory Group for Aerospace Research and Development, North Atlantic Treaty Organization, Neuilly sur Seine, France, 1987), pp. 42–45.
[44]Y. Awatsuji, M. Sasada, and T. Kubota, "Parallel quasi-phase-shifting digital holography," Appl. Phys. Lett. **85**(6), 1069–1071 (2004).
[45]T. Onuma and Y. Otani, "A development of two-dimensional birefringence distribution measurement system with a sampling rate of 1.3 MHz," Opt. Commun. **315**, 69–73 (2014).
[46]K. Yatabe, K. Ishikawa, and Y. Oikawa, "Simple, flexible, and accurate phase retrieval method for generalized phase-shifting interferometry," J. Opt. Soc. Am. A **34**(1), 87–96 (2017).
[47]K. Yatabe, K. Ishikawa, and Y. Oikawa, "Hyper ellipse fitting in subspace method for phase-shifting interferometry: Practical implementation with automatic pixel selection," Opt. Express **25**(23), 29401–29416 (2017).
[48]H. Schreiber and J. H. Bruning, "Phase shifting interferometry," in *Optical Shop Testing*, 3rd ed. (John Wiley & Sons, Ltd., Hoboken, NJ, 2006), pp. 623–629.
[49]K. Yatabe, R. Tanigawa, K. Ishikawa, and Y. Oikawa, "Time-directional filtering of wrapped phase for observing transient phenomena with

https://doi.org/10.1121/10.0022537

parallel phase-shifting interferometry," Opt. Express **26**(11), 13705–13720 (2018).
[50]T. Miyachi, "Low-noise moving model test facility completed at RTRI," Ascent **9**, 22 (2021).
[51]Y. Makino, Y. Takano, M. Akutsu, and T. Uda, "Measurement of radiated sound directivity of moving sources at low Mach numbers," in *INTER-NOISE and NOISE-CON Congress and Conference Proceedings, Internoise23* (2023) (I-INCE, Luzern, Switzerland, 2023), No. 3–7–9.
[52]Z. Zhang, "A flexible new technique for camera calibration," IEEE Trans. Pattern Anal. Mach. Intell. **22**(11), 1330–1334 (2000).
[53]S. Wei and S. Ma, "Explicit camera calibration: Theory and experiments," IEEE Trans. Pattern Anal. Mach. Intell. **16**(5), 469–480 (1994).
[54]J. Heikkilä and O. Silvén, "A four-step camera calibration procedure with implicit image correction," in *Proceedings of the IEEE Computer Society Conference on Computer Vision and Pattern Recognition* (IEEE, New York, 1997), pp. 1106–1112.